Title	Evaluation of a multiscale modelling methodology to predict the mechanical properties of PCL/-TCP sintered scaffold materials
Author(s)	Doyle, Heather; Lohfeld, Stefan; McDonnell, Pat; McHugh, Peter E.
Publication Date	2014-12-02
Publication Information	Doyle, Heather, Lohfeld, Stefan, McDonnell, Pat, & McHugh, Peter. (2015). Evaluation of a Multiscale Modelling Methodology to Predict the Mechanical Properties of PCL/-TCP Sintered Scaffold Materials. Annals of Biomedical Engineering, 43(8), 1989-1998. doi: 10.1007/s10439-014-1199-x
Publisher	Springer Verlag
Link to publisher's version	http://dx.doi.org/10.1007/s10439-014-1199-x
Item record	http://hdl.handle.net/10379/6029
DOI	http://dx.doi.org/10.1007/s10439-014-1199-x

The original publication was published in the Annals of Biomedical Engineering (2015) 43: 1989.
The final publication is available at Springer via http://dx.doi.org/10.1007/s10439-014-1199-x

Title: Evaluation of a multiscale modelling methodology to predict the mechanical properties of PCL/β-TCP sintered scaffold materials.

Abbreviated Title: Evaluation of multiscale modelling of SLS materials

Author Names: Heather Doyle[a]; Stefan Lohfeld, Dr [a]; Pat McDonnell, Dr [a]; Peter McHugh, Prof.[a]

Author Affiliations: [a]Biomechanics Research Centre (BMEC), Mechanical and Biomedical Engineering, National University of Ireland, Galway

Corresponding Author:

Email: heatherdoylenuig@gmail.com

1 Abstract

A multiscale modelling methodology to predict the macroscale stiffness of selective laser sintered polycaprolactone (PCL)/β-tricalcium phosphate (β-TCP) materials is evaluated. The relationship between a micromechanics-evaluated composite material elastic modulus (E_{eff}) and segment grey-value (GV_{ave}) is established for a 90/10wt% PCL/β-TCP material and compared to the previously established E_{eff} versus GV_{ave} relationship for a 50/50wt% PCL/β-TCP material. The increase in E_{eff} with GV_{ave} was found to be greater for the 90/10wt% material than for the 50/50wt% material. Differences in the material microstructures are visible with greater local conglomerations of β-TCP in the 90/10wt% material compared to the 50/50wt% material. These results indicate that the relationship between E_{eff} and GV_{ave} is material-specific and that one definition cannot be used to describe both materials. We have used the E_{eff} and GV_{ave} relationship specific to the 90/10wt% material to assign element-specific elastic properties in a high resolution macroscale strut finite element model to successfully predict the experimentally-evaluated strut effective stiffness of the 90/10wt%. These results combined indicate that this multiscale modelling methodology accurately predicts the effective elastic modulus of SLS struts with different material configurations, and that it can be used to determine the material-specific definition of the relationship between E_{eff} and GV_{ave} for a particular material.

Keywords: selective laser sintering; polycaprolactone, B-tricalcium phosphate; micromechanical modelling; bone tissue engineering; mechanical properties; finite element analysis.

2 Introduction

Selective laser sintering (SLS) is a rapid prototyping method where a laser is used to sinter/melt a powdered material one layer at a time in a computer-generated pattern to build up a 3D part. Advantages of this fabrication method are a high degree of repeatability and conformity to the original design, the flexibility of design possibilities and the range of materials that can be used, including polymers[29,42,15,17,38], polymer-ceramic composites[9,12,13,22,36,43] and metals[26,37]. The fabrication of ceramic composite materials using SLS can result in complex material microstructures that are influenced by many factors including particle size, laser power and ceramic content[9,17,22,43].

The purpose of the incorporation of ceramic particles in polymer-based ceramics is traditionally to improve material properties by reinforcing the polymer phase, in particular to increase the material elastic modulus[3,7]. However, in the case of SLS-fabricated composite materials, the ceramic phase has been shown to act as a barrier to sintering, requiring increased laser power for sintering[22]. This is due to the difference in sintering temperatures of the polymer and ceramic phases. Sintering of this type of composite material is carried out at temperatures above the melt temperature of the polymer phase but below the melt temperature of the ceramic phase. Therefore the ceramic particles do not get sintered, and act to inhibit the flow and consolidation of the polymer melt. β-Tricalcium Phosphate (β-TCP) particles are commonly included in orthopaedic scaffolding materials as they have good biocompatibility and osteoconductivity, both on their own and in combination with polymers[10,19,21,24,30,41]. While the inclusion of large volumes of β-TCP in polymeric scaffolds is desirable to promote osteoconductivity, the effect of this on the resulting scaffold material properties must be considered.

Finite element models using 3D CAD geometries have proven to be unable to capture the mechanical behaviour of this type of SLS-fabricated scaffold[5,40] due to the fact that CAD models can only account for the intended scaffold macroporosity but cannot account for any scaffold microporosity or surface roughness that occur as a result of the fabrication process. High resolution finite element meshes generated from micro-chromatography (μ-CT) scans of bone tissue engineering scaffolds can overcome this by accurately capturing real scaffold geometries on the macroscale and microscale[6,8,25,32–34,40]. A methodology to generate effective elastic properties on the microscale of 50/50wt% Polycaprolactone (PCL)/β-TCP SLS materials using microstructural modelling methods was established in a previous study carried out by the authors[11]. Heterogeneous material property assignment based on element grey-value was applied in high resolution full strut FE models (macroscale) generated from μ-CT scans, resulting in an accurate prediction of the experimentally obtained strut elastic modulus. Pixel grey-value refers to the intensity of a pixel on a μ-CT scan image.

The overall goals of this study are to test the capabilities of the previously developed micromechanical modelling methodology by applying it to a similar material with a different polymer-ceramic ratio. Specifically, the first objective of this study is to establish whether the relationship between the material elastic modulus and average grey-value on the microscale is the same for SLS materials with different volumes of β-TCP particles. The second objective of this study is to test the ability of this methodology to predict the macroscale strut effective modulus of the materials. The validity of these models is assessed by comparing the predicted macroscale strut effective modulus of 90/10wt% PCL/β-TCP struts with the experimentally evaluated strut modulus.

3 Materials and Methods

3.1 Materials, Fabrication & Tensile Testing

Poly-ε-caprolactone (PCL) powder (CAPA6506, Solvay, UK) with a powder particle diameter of 600 μm was cryogenically milled to particles sizes of 0 - 110 μm, without the use of additives, at Noll Aufbereitungstechnologie GmbH (Bobingen, Germany). The particle size distribution for particle sizes with diameter 0 - 110 μm was measured by Noll Aufbereitungstechnologie GmbH giving values of $D_{10\%}$ = 16.10 μm, $D_{50\%}$ = 42.86 μm (median particle size), and $D_{90\%}$ = 76.42 μm. This powder was then sieved to separate particles with diameter 0 – 50 μm and 50 – 110 μm. PCL powder with a particle size of 50 – 110 μm and β-tricalcium phosphate (β-TCP) (Fluka) with a particle size of 3 – 5 μm were mixed in a 90:10wt% ratio (approximately 5 vol% β-TCP) using a hand mixer for five minutes until well blended to give a 90/10wt% PCL/β-TCP powder mix. This PCL particle size is the same as used in the fabrication of full 90/10wt% scaffolds by Lohfeld et al.[23]. Individual struts with a rectangular cross section of 0.77 mm x 0.55 mm and length of 13 mm were fabricated in ladders of struts using SLS with the Sinterstation 2500^{plus} system (DTM, USA). In short, the outline scan method[10] was used to achieve a small strut cross section. A laser power of 7 W was used, with a laser spot diameter of 410 μm, laser scan speed of 1778 mm/s, part bed temperature of 49°C and powder layer thickness of 0.11 mm.

The elastic modulus of the 90/10wt% PCL/β-TCP struts was evaluated using uniaxial tensile testing on a Zwick biaxial testing machine at a strain rate of 1% of the gauge length per minute. Tensile samples were prepared by gluing each strut end inside small, stiff plastic tubes (outer diameter 2.5 mm, wall thickness 0.4 mm) using a gel cyanoacrylate adhesive (Loctite® Power Easy™). The plastic tubes were then gripped directly to prevent damage to the strut at the grips. Strain was measured using a calibrated video extensometer camera and dimensions were measured prior to testing using the calibrated video extensometer camera. Tensile tests were carried out as per ISO 527-1.

3.2 Structural and Morphological Characterization

High resolution scans of the 90/10wt% single scaffold struts (macroscale scan) were obtained using a micro-computed tomography (μ-CT) scanner (SkyScan-1072 High-resolution desk-top micro-CT system, University of Aberdeen, UK) with a voxel size of 14.65 μm. In addition a higher resolution scan of the 90/10wt% material (microscale scan) was obtained from a small segment of a 90/10wt% strut (approximate dimensions 0.77 mm x 0.1 mm x 0.1 mm) using X-ray microtomography (XMT) (phoenix nanotom®, GE, at SEAM, Waterford Institute of Technology, Ireland) with a voxel size of 0.83 μm. All scanning was carried out on struts that had not been tensile tested but that were fabricated in the same batch as the tensile specimens in Section 3.1.

3.3 Micromechanical Analysis

A micromechanical study was conducted to determine the relationship between material modulus (E_{eff}) and average grey-value (GV_{ave}) on the microscale. FE models of cuboidal material segments were generated from the microscale scan (voxel size 0.83 μm) using Mimics software with segment dimensions approximately equal to one element in the full strut models in Section 3.4 (edge length 29.05 μm). The PCL and β-TCP phases were represented as separate materials in one meshed part and the average CT scan grey-value was calculated for each segment. A FE mesh with 8-noded hexahedral voxel elements with reduced integration was generated for each segment. Linear elastic material properties and a Poisson's ratio of 0.3 were assumed for both phases. The elastic modulus of cast PCL (E_{PCL} = 277 MPa[11]) and a β-TCP elastic modulus ($E_{\beta\text{-}TCP}$) of 24.6 GPa were assumed[39]. Abaqus/Standard V6.10 was used for all simulations. A total of 21 segment models were generated, with average segment grey-values ranging from 100 to 141. These were divided

into seven groups based on GV_{ave}, with three segments per group in order to represent possible variations in material composition.

The "windowing approach" as described for example in references [2,18,27] was used to determine the effective elastic modulus of each segment. The windowing approach involves the application of three types of uniform boundary conditions: kinematic, static and mixed uniform boundary conditions. For kinematic uniform boundary conditions (KUBC) a macroscopically homogeneous strain tensor, $\boldsymbol{\varepsilon}$, is imposed on all boundaries, whereas for static uniform boundary conditions (SUBC) a macroscopically homogeneous stress tensor, $\boldsymbol{\sigma}$, is imposed on all boundaries. Mixed uniform boundary conditions (MUBC) are a combination of KUBC and SUBC. Boundary conditions are only assigned to the faces perpendicular to the loading direction allowing the other four faces to freely deform, resulting in zero stresses and non-zero strains on non-loaded faces. We have established in our previous study that E_{eff} evaluated using MUBC falls between E_{eff} evaluated using KUBC and SUBC, and that it can be used to predict the macroscale elastic properties of sintered struts[11]. For this reason, MUBC are used to evaluate E_{eff} in this study.

MUBC were applied to each segment and tensile simulations in 1-, 2- and 3-directions as well as shear simulations in the 1-2, 2-3 and 3-1 planes were carried out for each segment. The effective isotropic elastic modulus E_{eff} was evaluated for each segment using strain energy density equivalence. The strain energy density (U) for each deformed configuration was calculated using Equation (1):

$$U = \frac{1}{2}\{\sigma_{11}\varepsilon_{11} + \sigma_{22}\varepsilon_{22} + \sigma_{33}\varepsilon_{33} + \sigma_{12}\gamma_{12} + \sigma_{23}\gamma_{23} + \sigma_{31}\gamma_{31}\} \quad (1)$$

where σ_{11} is the volume average stress in the 1-direction, σ_{12} is the volume average shear stress in the 1-2 plane, ε_{11} is the volume average strain in the 1-direction and γ_{12} is the volume average shear strain in the 1-2 plane with $\gamma_{12} = 2\ \varepsilon_{12}$. This can then be related to the

constitutive equations for a linear elastic material[3].The volume averaged stress $\langle \boldsymbol{\sigma} \rangle$ can be calculated as a function of volume averaged strain $\langle \boldsymbol{\varepsilon} \rangle$, E_{eff} and effective Poisson's ratio (υ_{eff}), are described by Equation (2).

$$\begin{bmatrix} \sigma_{11} \\ \sigma_{22} \\ \sigma_{33} \\ \sigma_{12} \\ \sigma_{23} \\ \sigma_{31} \end{bmatrix} = \frac{E_{\text{eff}}}{(1+\upsilon_{\text{eff}})(1-2\upsilon_{\text{eff}})} \begin{bmatrix} 1-\upsilon_{\text{eff}} & \upsilon_{\text{eff}} & \upsilon_{\text{eff}} & 0 & 0 & 0 \\ \upsilon_{\text{eff}} & 1-\upsilon_{\text{eff}} & \upsilon_{\text{eff}} & 0 & 0 & 0 \\ \upsilon_{\text{eff}} & \upsilon_{\text{eff}} & 1-\upsilon_{\text{eff}} & 0 & 0 & 0 \\ 0 & 0 & 0 & \frac{1-2\upsilon_{\text{eff}}}{2} & 0 & 0 \\ 0 & 0 & 0 & 0 & \frac{1-2\upsilon_{\text{eff}}}{2} & 0 \\ 0 & 0 & 0 & 0 & 0 & \frac{1-2\upsilon_{\text{eff}}}{2} \end{bmatrix} \begin{bmatrix} \varepsilon_{11} \\ \varepsilon_{22} \\ \varepsilon_{33} \\ \gamma_{12} \\ \gamma_{23} \\ \gamma_{31} \end{bmatrix} \quad (2)$$

E_{eff} can be re-written as Equation (3) for the case of uniaxial tension and Equation (4) for simple shear. Strain energy density and strain are averaged over a number of loading modes and directions to account for any possible directional variations in material mechanical properties. U_{uniax} is the average of U_{11}, U_{22} and U_{33}, U_{shear} is the average of U_{12}, U_{23} and U_{31}, $\varepsilon_{\text{uniax}}$ is the average of ε_{11}, ε_{22} and ε_{33} and γ_{shear} is the average of γ_{12}, γ_{23} and γ_{31}. Equations (3) and (4) below can be equated to solve for υ_{eff} (Equation (5)). Once evaluated, υ_{eff} can then be substituted back into Equation (3) or (4) to solve for E_{eff}.

$$E_{\text{eff}} = \frac{2U_{\text{uniax}}}{\varepsilon_{\text{uniax}}^{\,2}} \frac{(1+\upsilon_{\text{eff}})(1-2\upsilon_{\text{eff}})}{(1-\upsilon_{\text{eff}})} \quad (3)$$

$$E_{\text{eff}} = \frac{4U_{\text{shear}}}{\gamma_{\text{shear}}^{\,2}} (1+\upsilon_{\text{eff}}) \quad (4)$$

$$\upsilon_{\text{eff}} = \frac{\left(\frac{2U_{\text{shear}}}{\gamma_{\text{shear}}^{\,2}} - \frac{U_{\text{uniax}}}{\varepsilon_{\text{uniax}}^{\,2}}\right)}{\left(\frac{2U_{\text{shear}}}{\gamma_{\text{shear}}^{\,2}} - \frac{2U_{\text{uniax}}}{\varepsilon_{\text{uniax}}^{\,2}}\right)} \quad (5)$$

3.4 Computational Modelling of Full Strut Geometries

High resolution finite element (FE) models of the 90/10wt% full scaffold struts with a voxel size of 29.3 μm were generated from micro-CT scans using MIMICS software (Materialise, Belgium); the voxel size was reduced from 14.65 μm to reduce the computational cost of running the models. Reduced integration 8-noded hexahedral voxel elements were used for each strut model. Meshes were generated for four individual struts, and tensile tests of each scaffold strut were simulated to replicate the experimental test set-up as described in Section 3.1. Strain in the strut gauge length was calculated from the displacement of two nodes at a distance of 8 mm apart, representative of the measurement of nominal strain in experimental tensile tests of the 90/10wt% struts (Section 3.1). Nominal strain (ε) was calculated as the change in distance between these two nodes during the simulation and dividing by the original distance between these nodes. Stress (σ) was calculated as the total reaction force divided by the average cross-section area, and the strut effective modulus E was calculated as $E = \sigma / \varepsilon$.

The elastic modulus for each individual element of each strut model was assigned based on the grey-value of that element and the E_{eff} - GV_{ave} relationship generated using the micromechanical models (Figure 2), as described in Section 3.3. The element-specific modulus values were assigned to the full strut models based on GV_{ave} using MIMICS software (Materialise, Belgium). For comparison, simulations of all four strut geometries were carried out where the elastic modulus value of cast PCL (E_{PCL} = 277MPa[11]) was uniformly assigned to the individual elements in each strut. It should be noted that this method is not representative of the real material as it does not account for the β-TCP phase. However, as PCL constitutes approximately 95% of the volume of this material it is anticipated that that the material properties of the PCL component would dominate the

overall strut mechanical behaviour, therefore E_{PCL} is included for comparison purposes. In all cases isotropic linear elastic constants were used with a Poisson's ratio $\upsilon = 0.3$[14].

3.5 Degree of Anisotropy

Isotropic elastic properties are assumed in all macroscale full strut models (Section 4) as the voxel grey-value is the only information available, i.e. no directional information is available. In order to validate assumption of isotropy the degree of anisotropy (A) of the microscale segment models was calculated using the method outlined by Kanit et al.[20] where anisotropy is calculated as a function of the 3D material stiffness matrix $\boldsymbol{C}$, as opposed to calculating anisotropy in a given plane as is common elsewhere[1,16,28,35]. Simulations of seven micromechanical segments of the 90/10wt% material, one segment from each average grey-value range, were carried out using KUBC[20]. The value of A of segments of the 50/50wt% material used in a previous study[11] were also evaluated for comparison purposes. The anisotropy value is calculated from Equation 7, where Y_{11}, Y_{12} and Y_{44} are calculated from $\boldsymbol{C}$ (Equation 6) using Equations 8-10, where $A = 1$ for an isotropic material.

$$\begin{bmatrix}\sigma_{11}\\ \sigma_{22}\\ \sigma_{33}\\ \sigma_{12}\\ \sigma_{23}\\ \sigma_{31}\end{bmatrix} = \begin{bmatrix} C_{11} & C_{12} & C_{13} & C_{14} & C_{15} & C_{16} \\ & C_{22} & C_{23} & C_{24} & C_{25} & C_{26} \\ & & C_{33} & C_{34} & C_{35} & C_{36} \\ & & & C_{44} & C_{45} & C_{46} \\ & & & & C_{55} & C_{56} \\ & & & & & C_{66} \end{bmatrix} \begin{bmatrix}\varepsilon_{11}\\ \varepsilon_{22}\\ \varepsilon_{33}\\ \gamma_{12}\\ \gamma_{23}\\ \gamma_{31}\end{bmatrix} \tag{6}$$

$$A = \frac{2Y_{44}}{Y_{11} - Y_{12}} \tag{7}$$

$$Y_{11} = \frac{C_{11} + C_{22} + C_{33}}{3} \tag{8}$$

$$Y_{12} = \frac{C_{12} + C_{23} + C_{13}}{3} \tag{9}$$

$$Y_{44} = \frac{C_{44} + C_{55} + C_{66}}{3} \tag{10}$$

4 Results

4.1 Materials, Fabrication and Tensile Testing

Single bone tissue engineering scaffold struts were successfully fabricated from a 90:10wt% PCL/β-TCP powder mixture using SLS. The experimentally determined elastic modulus of the 90:10wt% struts was found to be 123.51 ± 30.20 MPa (n = 16). The experimentally determined elastic modulus of 50/50wt% struts was evaluated in a previous study giving 98.87 ± 22.59 MPa (n = 7) [11].

4.2 Structural and Morphological Characterization

High resolution CT scan images of the 90/10wt% material are shown in comparison with CT scan images for the 50/50wt% material generated in a previous study[11] in Figure 1, showing inhomogeneous microstructures for both 90/10wt% and 50/50wt% SLS materials. The β-TCP content and particle sizes in the 90/10wt% struts are the same size as the powder particles used to fabricate full 90/10wt% PCL/β-TCP scaffolds for an in vivo study by Lohfeld et al.[23], whereas a reduced PCL particle size of 0 – 50 μm was required for the fabrication of 50/50wt% PCL/β-TCP struts in order to achieve sintering with increased β-TCP content[11]. A smaller volume of individual β-TCP particles are visible in the scan image of the 90/10wt% material, as expected from the lower % composition in this material. Small agglomerations of β-TCP are visible as bright regions and porous regions are visible as darker regions in both scan images. The small β-TCP particles in the 90/10wt% material are located along the outside of the larger PCL particles and in ‘seams’ along the interface between sintered PCL particles in fully-sintered regions. In contrast, the small β-TCP particles in the 50/50wt% material are more interspersed throughout the material, likely as a result of the smaller PCL particles.

4.3 Micromechanical Modelling Results

Micromechanical modelling results for the 90/10wt% material, carried out for 21 segments using MUBC, are presented in Figure 2. The average E_{eff} for each grey-value level was calculated and the line fit in Figure 2 gives a linear relationship between E_{eff} and GV_{ave}. This established relationship between E_{eff} and GV_{ave} for the 90/10wt% material is shown in Figure 3 in comparison to the equivalent relationship for the 50/50wt% material established in our previous publication[11]. The slope is greater for the 90/10wt% material, indicating that the change in E_{eff} with increasing GV_{ave} is greater for the 90/10wt% material than the 50/50wt% material.

4.4 Full Strut Modelling

Full strut FE models were successfully generated for the 90/10wt% full scaffold struts using Mimics software. Section view images of the strut FE model geometry of a 90/10wt% strut and a 50/50wt% strut are shown in Figure 6, with regions of stiff material highlighted by a lighter grey and regions of softer materials marked by darker greys. A greater amount of porosity along the loading axis is visible in the 50/50wt% strut than the 90/10wt% strut. The volume percentage of elements within each grey-value range for each strut model type is shown in Figure 7. A similar distribution of elements are observed for each material however the greatest percentage of elements in the 90/10wt% struts are at a grey-value of approximately 100, whereas the greatest percentage of elements in the 50/50wt% struts have a lower grey-value of approximately 70.

The experimentally evaluated elastic modulus of the 90/10wt% struts and the 0/50wt% struts are given in Section 4.1. The strut effective modulus calculated from tensile simulations of the 90/10wt% struts with a range of input mechanical properties are shown in comparison with the experimental strut modulus in Figure 8. Analysis of the results show no statistical

difference between the experimental strut modulus and the effective strut modulus of the 90/10wt% struts (n = 4) evaluated using the microstructure-based method when compared using a Mann-Whitney test (p-value = 0.1190). A non-parametric test was used due to low sample numbers. The use of homogeneous PCL elastic properties (n = 4) does not give an accurate prediction of the strut effective modulus for the 90/10wt% struts (p-value = 0.0029), therefore the use of microstructure-based material property assignment is more accurate than the use of PCL elastic properties for the 90/10wt% struts. The computational and experimental strut effective modulus of the 50/50wt% struts generated in our previous study[11] are included for comparison purposes. Results for the 50/50wt% struts show no statistical difference between the experimental strut modulus and the effective strut modulus (n = 4) evaluated using the microstructure-based method when compared using a Mann-Whitney test (p-value = 0.0726). Overall, the use of homogeneous PCL properties was shown to overestimate the strut effective modulus. The heterogeneously assigned material properties generated from micromechanical modelling give the most accurate prediction of strut elastic modulus.

4.5 Degree of Anisotropy

The degree of anisotropy was calculated for micromechanical segments of both the 90/10wt% material used in this study and the 50/50wt% material presented in a previous study. The results for both materials are shown in Figure 4 with respect to GV_{ave} (left) and volume % of β-TCP. These results indicate that the segment models for both materials are generally close to isotropy ($A = 1$), with an average of $A = 1.11$ for the 90/10wt% material and $A = 1.02$ for the 50/50wt% material. Representative segment model geometries for segments containing small and larger quantities of β-TCP are presented in Figure 5 for each material, showing the values of A for each segment.

5 Discussion

The first objective of this study was to determine whether the relationship between E_{eff} and GV_{ave} is the same for SLS materials with different volumes of β-TCP. It is clear from Figure 3 that this is not the case. The increase in E_{eff} with increasing grey-value is greater for the 90/10wt% material than for the 50/50wt% material and therefore the GV_{ave} - E_{eff} relationship is specific to each material. This is likely due to the influence of the different material compositions on sintering conditions and the resulting material microstructures (Figure 1). Segments of the 90/10wt% material have a larger difference between E_{eff} at low and high values of GV_{ave} as the local conglomerations or 'seams' of β-TCP have a high E_{eff}, compared to the surrounding regions of PCL. In contrast, segments of the 50/50wt% material with high β-TCP content tend to have β-TCP particles dispersed throughout the PCL matrix and as a result there is a smaller difference between E_{eff} at low and high values GV_{ave}.

The degree of anisotropy (A)[20] of the micromechanical segments was calculated to evaluate if the use of isotropic elastic moduli is appropriate. The segment models for both materials are generally close to isotropy (A = 1), with average values of $A_{90/10wt\%}$ = 1.11 and $A_{50/50wt\%}$ = 1.02. This verifies our assumption of isotropy for full strut FE models where anisotropy cannot be applied for the simple reason that the only element information available is grey-value and that no directional information is available. Segments generated from the 90/10wt% material are slightly less isotropic than segments generated from the 50/50wt% material, Figure 4, due to the presence of 'seams' of β-TCP along one direction in the 90/10wt% material, for example along the front-facing side of the segment in the top right of Figure 5.

The second objective of this study was to determine the ability of this multiscale methodology to predict the macroscale strut effective modulus of these SLS materials. The

micromechanical approach to elastic modulus assignment in the full strut simulations gives a more accurate estimate of strut modulus compared to uniform homogeneous elastic modulus values, as shown by comparisons with E_{PCL} in Figure 8. In full strut simulations with homogeneous PCL elastic modulus (Figure 8) the effect of macropores and surface roughness are accounted for by the high resolution strut mesh but microscale features are not. Using the modulus values presented in Figure 8, the ratio of the 90/10wt% strut modulus to the 50/50wt% strut modulus is 1.77 when homogeneous PCL elastic properties are used. This indicates the large effect that the increased number of macropores in the 50/50wt% struts (Figure 6) has on reducing the overall strut modulus. However, the value for the 90/10wt% strut modulus is much higher than the experimentally determined value due to the fact that strut microporosity is not accounted for in these models, i.e. the modulus for solid, cast PCL is assigned uniformly to all elements.

In full strut simulations where the micromechanics-derived elastic moduli are applied (Figure 8) the effect of the macropores and the microscale features are accounted for giving a much better representation of the overall material behaviour. The microscale features that are captured include the microporosity of the sintered material, which has the effect of reducing the strut modulus compared to the homogeneous PCL properties, and also the reinforcing effect of the β-TCP particles. For these strut models, the ratio of the 90/10wt% strut modulus to the 50/50wt% strut modulus is 1.23, which is close to the value of 1.25 for the experimental results and considerably less than that of the homogeneous PCL models (1.77). This is due to the incorporation of the microscale features in the micromechanical models. Specifically, for the 90/10wt% struts, the microporosity of the sintered material has the effect of reducing the overall strut modulus while reinforcing effect of the 10wt% β-TCP is relatively small. For the 50/50wt% struts, again the microporosity of the sintered material has the effect of reducing the strut modulus but the reinforcing effect of the 50wt% β-TCP is

much greater than for the 90/10wt% material. For the 50/50wt% struts, it is the reinforcing effect which dominates, causing a slight increase in the overall strut modulus for the micromechanical model compared to the homogeneous model.

Although the modulus ratio between the 90/10wt% and 50/50wt% strut moduli for the micromechanical models agrees quite well with the experimental results, the absolute values of the strut modulus are approximately 25% higher in both cases. This may be due to the value of the PCL modulus that was chosen for the micromechanical modelling (E_{PCL} = 277 MPa[11]) which was based on tensile testing of cast PCL material. It is possible that the modulus of cast PCL is higher than that of PCL which is processed by laser sintering, which would have the effect of increasing the strut elastic modulus in the model results presented in Figure 8. The exact processing conditions of PCL during sintering (temperature, duration of exposure etc.) are not known. However, it should be noted that in order to replicate the conditions as closely as possible, the same PCL powder was used to create the PCL tensile samples and the sintered struts, and a vacuum melt temperature of 120°C was used as per a study by Roosa et al. in which solid PCL samples were fabricated using vacuum moulding[31].

The results of this study have established that the relationship between E_{eff} and average segment grey-value of composite SLS materials is specific to each material configuration and that a 'one size fits all' definition does not apply. We have used the methodology established in our previous study[11] to generate a material-specific definition of the relationship between E_{eff} and average segment grey-value for the 90/10wt% PCL/β-TCP material. This relationship has been shown to successfully predict the stiffness of 90/10wt% PCL/β-TCP struts by using grey-value specific assignment of elastic properties in full strut simulations. The μ-CT approach to full SLS strut modelling captures variations due to macroscale features, i.e. macropores and surface roughness, through the use of μ-CT derived high resolution macroscale FE meshes. Microscale features such as microporosity and the presence of β-TCP

particles are accounted for in models where the μ-CT derived micromechanical elastic modulus is applied. This would not be possible with CAD based FE modelling, as neither macroscale nor microscale features would be accounted for.

These results indicate that the multiscale modelling framework described here and in our previous publication[11] can accurately capture the effective elastic modulus of SLS struts of different materials, but that a material-specific definition of the relationship between microscale stiffness and grey-value is required. This can be achieved using the microstructure-based modelling method presented here and in our previous study[11]. In conclusion, the main result of this study is that this multi-scale methodology can predict the macroscale properties of this type of material, that it can be used to generate the specific set of constants that is required for a particular material.

6 Acknowledgements

H.Doyle acknowledges funding from the Irish Research Council under the Embark Initiative Postgraduate Research Scholarship Scheme. The authors would like to acknowledge the SFI/HEA funded Irish Centre for High End Computing for the provision of computational resources and support.

7 References

1. Baron, C., M. Talmant, and P. Laugier. Effect of porosity on effective diagonal stiffness coefficients (cii) and elastic anisotropy of cortical bone at 1 MHz: A finite-difference time domain study. *J. Acoust. Soc. Am.* 122:1810, 2007.

2. Böhm, H. J. A Short Introduction to Continuum Micromechanics. In: Mechanics of Microstructured Materials, edited by H. J. Bohm. Vienna: CISM Courses and Lectures, Springer-Verlag, 2004, pp. 1–40.

3. Borbély, A., P. Kenesei, and H. Biermann. Estimation of the effective properties of particle-reinforced metal – matrix composites from microtomographic reconstructions. *Acta Mater.* 54:2735–2744, 2006.

4. Bower, A. F. Applied Mechanics of Solids. , 2008.at <http://solidmechanics.org/text/Chapter3_2/Chapter3_2.htm>

5. Cahill, S., S. Lohfeld, and P. E. McHugh. Finite element predictions compared to experimental results for the effective modulus of bone tissue engineering scaffolds fabricated by selective laser sintering. *J. Mater. Sci. Mater. Med.* 20:1255–62, 2009.

6. Charles-Harris, M., S. del Valle, E. Hentges, P. Bleuet, D. Lacroix, and J. a Planell. Mechanical and structural characterisation of completely degradable polylactic acid/calcium phosphate glass scaffolds. *Biomaterials* 28:4429–38, 2007.

7. Chawla, N., R. S. Sidhu, and V. V Ganesh. Three-dimensional visualization and microstructure-based modeling of deformation in particle-reinforced composites. *Acta Mater.* 54:1541–1548, 2006.

8. Van Cleynenbreugel, T., J. Schrooten, H. Van Oosterwyck, and J. Vander Sloten. Micro-CT-based screening of biomechanical and structural properties of bone tissue engineering scaffolds. *Med. Biol. Eng. Comput.* 44:517–25, 2006.

9. Das, S. Selective Laser Sintering of Polymers and Polymer-Ceramic Composites. In: Virtual Prototyping & Bio Manufacturing in Medical Applications. 2008, pp. 226–260.doi:10.1007/978-0-387-68831-2_11

10. Dong, J., T. Uemura, Y. Shirasaki, and T. Tateishi. Promotion of bone formation using highly pure porous beta-TCP combined with bone marrow-derived osteoprogenitor cells. *Biomaterials* 23:4493–502, 2002.

11. Doyle, H., S. Lohfeld, and P. McHugh. Predicting the Elastic Properties of Selective Laser Sintered PCL/β-TCP Bone Scaffold Materials Using Computational Modelling. *Ann. Biomed. Eng.* 42:661–77, 2013.

12. Eosoly, S., D. Brabazon, S. Lohfeld, and L. Looney. Selective laser sintering of hydroxyapatite/poly-epsilon-caprolactone scaffolds. *Acta Biomater.* 6:2511–7, 2010.

13. Eosoly, S., N. E. Vrana, S. Lohfeld, M. Hindie, and L. Looney. Interaction of cell culture with composition effects on the mechanical properties of polycaprolactone-hydroxyapatite scaffolds fabricated via selective laser sintering (SLS). *Mater. Sci. Eng. C* 32:2250–2257, 2012.

14. Eshraghi, S., and S. Das. Mechanical and microstructural properties of polycaprolactone scaffolds with one-dimensional, two-dimensional, and three-dimensional orthogonally oriented porous architectures produced by selective laser sintering. *Acta Biomater.* 6:2467–76, 2010.

15. Franco, A., M. Lanzetta, and L. Romoli. Experimental analysis of selective laser sintering of polyamide powders: an energy perspective. *J. Clean. Prod.* 18:1722–1730, 2010.

16. Gassan, J., A. Chate, and A. K. Bledzki. Calculation of elastic properties of natural fibers. *J. Mater. Sci.* 6:3715–3720, 2001.

17. Goodridge, R. D., C. J. Tuck, and R. J. M. Hague. Laser sintering of polyamides and other polymers. *Prog. Mater. Sci.* 57:229–267, 2012.

18. Hazanov, S. Hill condition and overall properties of composites. *Arch. Appl. Mech.* 68:385–394, 1998.

19. Kang, Y., A. Scully, D. a Young, S. Kim, H. Tsao, M. Sen, and Y. Yang. Enhanced mechanical performance and biological evaluation of a PLGA coated β-TCP composite scaffold for load-bearing applications. *Eur. Polym. J.* 47:1569–1577, 2011.

20. Kanit, T., F. N'Guyen, S. Forest, D. Jeulin, M. Reed, and S. Singleton. Apparent and effective physical properties of heterogeneous materials : Representativity of samples of two materials from food industry. *Comput. Methods Appl. Mech. Eng.* 195:3960–3982, 2006.

21. Liu, G., L. Zhao, L. Cui, W. Liu, and Y. Cao. Tissue-engineered bone formation using human bone marrow stromal cells and novel beta-tricalcium phosphate. *Biomed. Mater.* 2:78–86, 2007.

22. Lohfeld, S., S. Cahill, V. Barron, P. McHugh, L. Dürselen, L. Kreja, C. Bausewein, and A. Ignatius. Fabrication, mechanical and in vivo performance of polycaprolactone / tricalcium phosphate composite scaffolds. *Acta Biomater.* 8:3446–3456, 2012.

23. Lohfeld, S., M. A. Tyndyk, S. Cahill, N. Flaherty, V. Barron, and P. E. McHugh. A method to fabricate small features on scaffolds for tissue engineering via selective laser sintering. *J. Biomed. Sci. Eng.* 03:138–147, 2010.

24. Lu, Z., and H. Zreiqat. Beta-tricalcium phosphate exerts osteoconductivity through alpha2beta1 integrin and down-stream MAPK/ERK signaling pathway. *Biochem. Biophys. Res. Commun.* 394:323–9, 2010.

25. Milan, J.-L., J. A. Planell, and D. Lacroix. Simulation of bone tissue formation within a porous scaffold under dynamic compression. *Biomech. Model. Mechanobiol.* 9:583–96, 2010.

26. Nakamoto, T., N. Shirakawa, Y. Miyata, and H. Inui. Selective laser sintering of high carbon steel powders studied as a function of carbon content. *J. Mater. Process. Technol.* 209:5653–5660, 2009.

27. Nemat-Nasser, S., and M. Hori. Micromechanics: Overall Properties of Heterogeneous Materials. North Holland, 1993.

28. Ni, Y., and M. Y. M. Chiang. Prediction of elastic properties of heterogeneous materials with complex microstructures. *J. Mech. Phys. Solids* 55:517–532, 2007.

29. Partee, B., S. J. Hollister, and S. Das. Selective Laser Sintering Process Optimization for Layered Manufacturing of CAPA® 6501 Polycaprolactone Bone Tissue Engineering Scaffolds. *J. Manuf. Sci. Eng.* 128:531, 2006.

30. Rai, B., J. L. Lin, Z. X. H. Lim, R. E. Guldberg, D. W. Hutmacher, and S. M. Cool. Differences between in vitro viability and differentiation and in vivo bone-forming efficacy of human mesenchymal stem cells cultured on PCL-TCP scaffolds. *Biomaterials* 31:7960–70, 2010.

31. Roosa, S. M. M., J. M. Kemppainen, E. N. Moffitt, P. H. Krebsbach, and S. J. Hollister. The pore size of polycaprolactone scaffolds has limited influence on bone regeneration in an in vivo model. *J. Biomed. Mater. Res. A* 92:359–68, 2010.

32. Saey, H., and D. W. Hutmacher. Application of micro CT and computation modeling in bone tissue engineering. *Comput. Des.* 37:1151–1161, 2005.

33. Sandino, C., and D. Lacroix. A dynamical study of the mechanical stimuli and tissue differentiation within a CaP scaffold based on micro-CT finite element models. *Biomech. Model. Mechanobiol.* 10:565–576, 2011.

34. Scheiner, S., R. Sinibaldi, B. Pichler, V. Komlev, C. Renghini, C. Vitale-Brovarone, F. Rustichelli, and C. Hellmich. Micromechanics of bone tissue-engineering scaffolds, based on resolution error-cleared computer tomography. *Biomaterials* 30:2411–9, 2009.

35. Sone, H., and M. D. Zoback. Mechanical properties of shale-gas reservoir rocks — Part 1: Static and dynamic elastic properties and anisotropy. *Geophysics* 78:D381–D392, 2013.

36. Tan, K. H., C. K. Chua, K. F. Leong, C. M. Cheah, P. Cheang, M. S. Abu Bakar, and S. W. Cha. Scaffold development using selective laser sintering of polyetheretherketone–hydroxyapatite biocomposite blends. *Biomaterials* 24:3115–3123, 2003.

37. Tolochko, N. K., M. K. Arshinov, A. V. Gusarov, V. I. Titov, T. Laoui, and L. Froyen. Mechanisms of selective laser sintering and heat transfer in Ti powder. *Rapid Prototyp. J.* 9:314–326, 2003.

38. Vitor, G., C. Henrique, and P. Klauss. Rapid Manufacturing of Polyethylene Parts With Controlled Pore Size Gradients Using Selective Laser Sintering. *Mater. Res.* 10:211–214, 2007.

39. Wang, C., X. Zhou, and M. Wang. Influence of sintering temperatures on hardness and Young's modulus of tricalcium phosphate bioceramic by nanoindentation technique. *Mater. Charact.* 52:301–307, 2004.

40. Williams, J. M., A. Adewunmi, R. M. Schek, C. L. Flanagan, P. H. Krebsbach, S. E. Feinberg, S. J. Hollister, and S. Das. Bone tissue engineering using polycaprolactone scaffolds fabricated via selective laser sintering. *Biomaterials* 26:4817–27, 2005.

41. Wongwitwichot, P., J. Kaewsrichan, K. H. Chua, and B. H. I. Ruszymah. Comparison of TCP and TCP/HA Hybrid Scaffolds for Osteoconductive Activity. *Open Biomed. Eng. J.* 4:279–85, 2010.

42. Yeong, W. Y., N. Sudarmadji, H. Y. Yu, C. K. Chua, K. F. Leong, S. S. Venkatraman, Y. C. F. Boey, and L. P. Tan. Porous polycaprolactone scaffold for cardiac tissue engineering fabricated by selective laser sintering. *Acta Biomater.* 6:2028–34, 2010.

43. Zhang, Y., L. Hao, M. M. Savalani, R. a Harris, and K. E. Tanner. Characterization and dynamic mechanical analysis of selective laser sintered hydroxyapatite-filled polymeric composites. *J. Biomed. Mater. Res. A* 86:607–16, 2008.

8 Figure Legends

Figure 1: CT scan images of high resolution scans of the 90/10wt% PCL/β-TCP material (left) and the 50/50wt% PCL/β-TCP from a previously published study[11] (right). β-TCP particles are visible as bright regions in the scans, with PCL material visible as grey regions and pores as dark regions in the scans.

Figure 2: Average effective isotropic elastic modulus (E_{eff}) versus average segment grey-value (GV_{ave}) for 90/10wt% PCL/β-TCP showing the linear relationship between E_{eff} and GV_{ave}.

Figure 3: Comparison of the E_{eff} versus average segment grey-value relationship for the 90/10wt% material and our previously published 50/50wt% material[11]. The dependence of segment E_{eff} on average grey-value is greater for the 90/10wt% material than for the 50/50wt% material.

Figure 4: Degree of anisotropy (A) versus average segment grey-value (left) and wt% β-TCP (right).

Figure 5: Representative micromechanical segment models for 90/10wt% PCL/β-TCP (top) and 50/50wt% PCL/β-TCP (bottom). β-TCP particle voxel elements are highlighted and the surrounding shaded and transparent grey regions represent PCL. The degree of anisotropy (A) and wt% β-TCP in each segment are indicated. The segment microstructure is shown for segments with values of A close to isotropy ($A = 1$) (left) and for segments with the anisotropic value of A (right).

Figure 6: Section view of 90/10wt% struts (top) and 50/50wt% struts (bottom) showing material property assignment. Differences in strut geometry are visible, with a greater amount of material in the loading direction for the struts with a lower volume of ceramic and visible pores in the loading direction in the struts with a higher volume of ceramic.

Figure 7: Element grey-value distribution in full strut FE models for both the 90/10wt% and 50/50wt% struts (average over four struts for each strut type).

Figure 8: Full strut computational model results for macroscale strut models of 90/10wt% and 50/50wt% PCL/β-TCP struts. Models using the micromechanical-evaluated material properties gave the best approximation of the experimental result (shown in red) for both strut types.

9 Figures

Figure 1

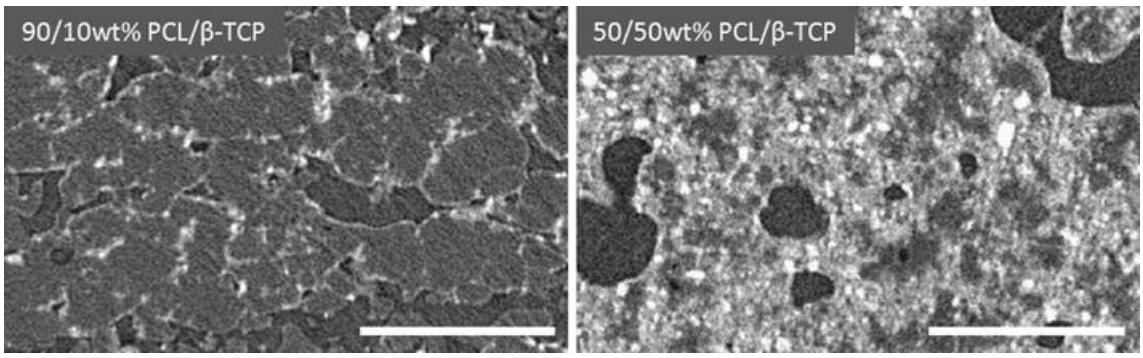

Figure 1: CT scan images of high resolution scans of the 90/10wt% PCL/β-TCP material (left) and the 50/50wt% PCL/β-TCP from a previously published study[11] (right). β-TCP particles are visible as bright regions in the scans, with PCL material visible as grey regions and pores as dark regions in the scans.

Figure 2

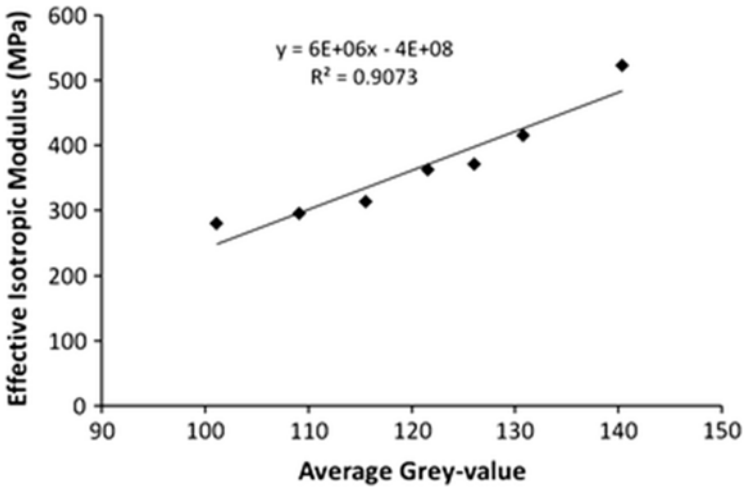

Figure 2: Average effective isotropic elastic modulus (E_{eff}) versus average segment grey-value (GV_{ave}) for 90/10wt% PCL/β-TCP showing the linear relationship between E_{eff} and GV_{ave}.

Figure 3

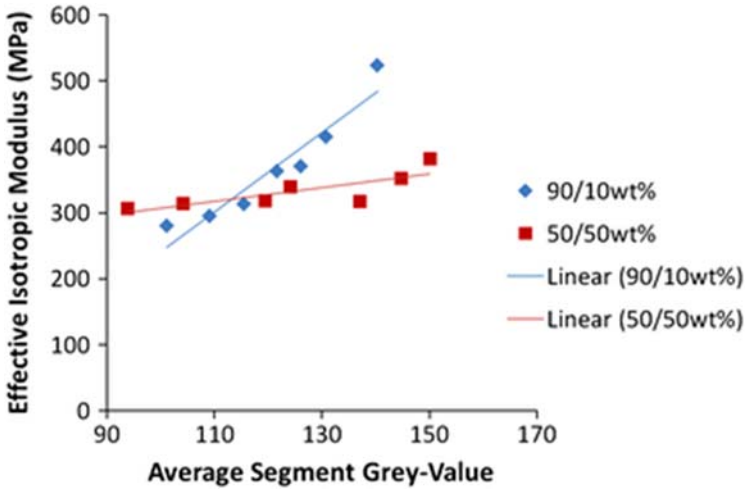

Figure 3: Comparison of the E_{eff} versus average segment grey-value relationship for the 90/10wt% material and our previously published 50/50wt% material[11]. The dependence of segment E_{eff} on average grey-value is greater for the 90/10wt% material than for the 50/50wt% material.

Figure 4

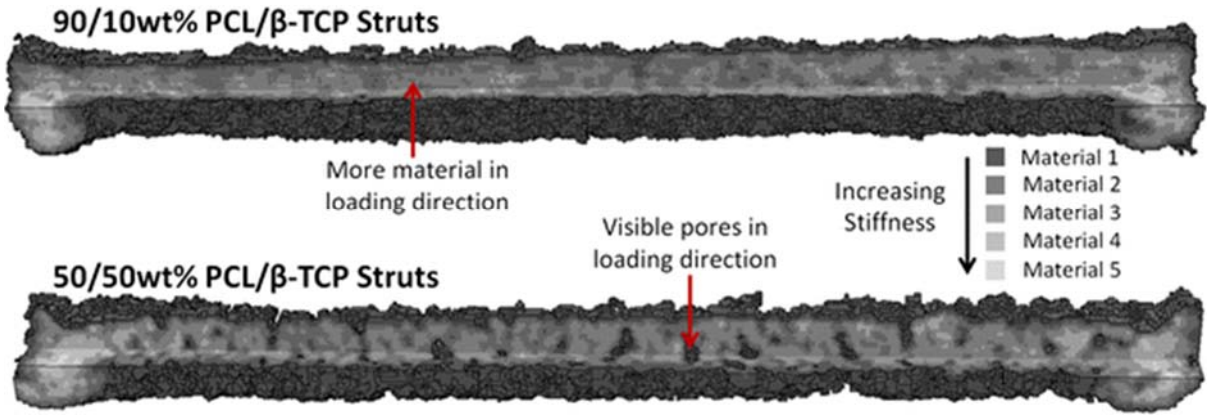

Figure 4: Degree of anisotropy (*A*) versus average segment grey-value (left) and wt% β-TCP (right).

Figure 5

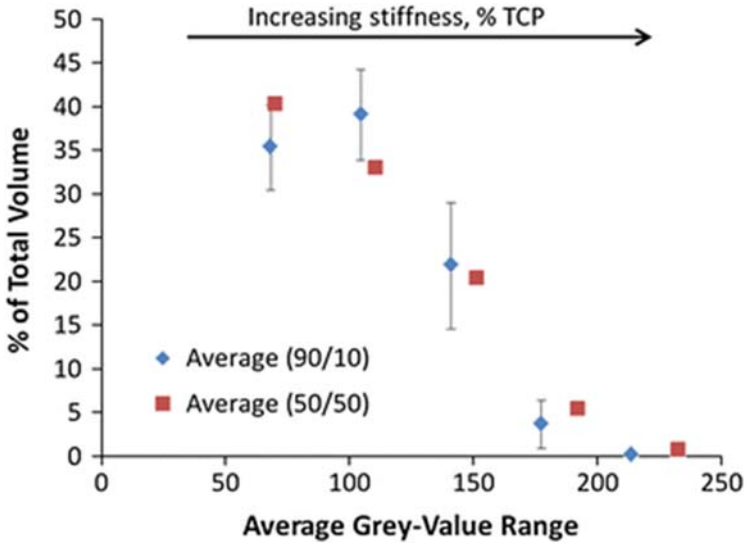

Figure 5: Representative micromechanical segment models for 90/10wt% PCL/β-TCP (top) and 50/50wt% PCL/β-TCP (bottom). β-TCP particle voxel elements are highlighted and the surrounding shaded and transparent grey regions represent PCL. The degree of anisotropy (*A*) and wt% β-TCP in each segment are indicated. The segment microstructure is shown for segments with values of *A* close to isotropy (*A* = 1) (left) and for segments with the anisotropic value of *A* (right).

Figure 6

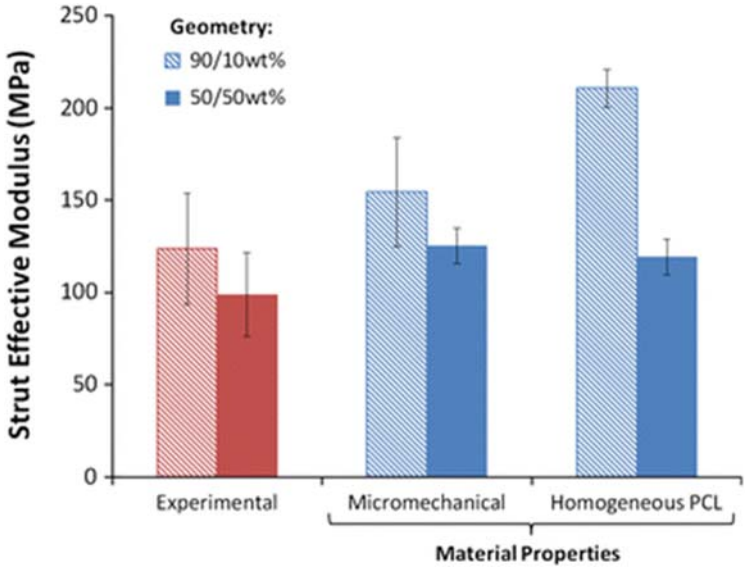

Figure 6: Section view of 90/10wt% struts (top) and 50/50wt% struts (bottom) showing material property assignment. Differences in strut geometry are visible, with a greater amount of material in the loading direction for the struts with a lower volume of ceramic and visible pores in the loading direction in the struts with a higher volume of ceramic.

Figure 7

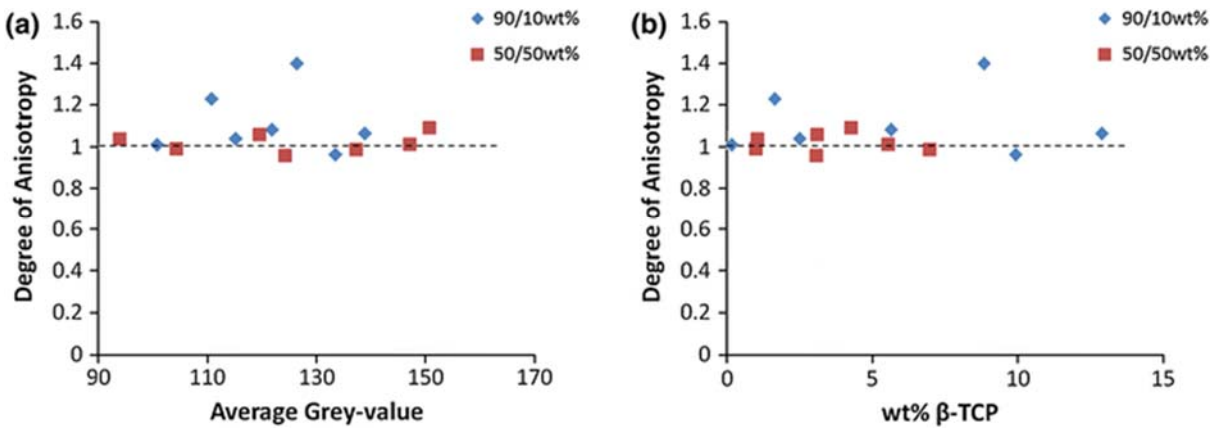

Figure 7: Element grey-value distribution in full strut FE models for both the 90/10wt% and 50/50wt% struts (average over four struts for each strut type).

Figure 8

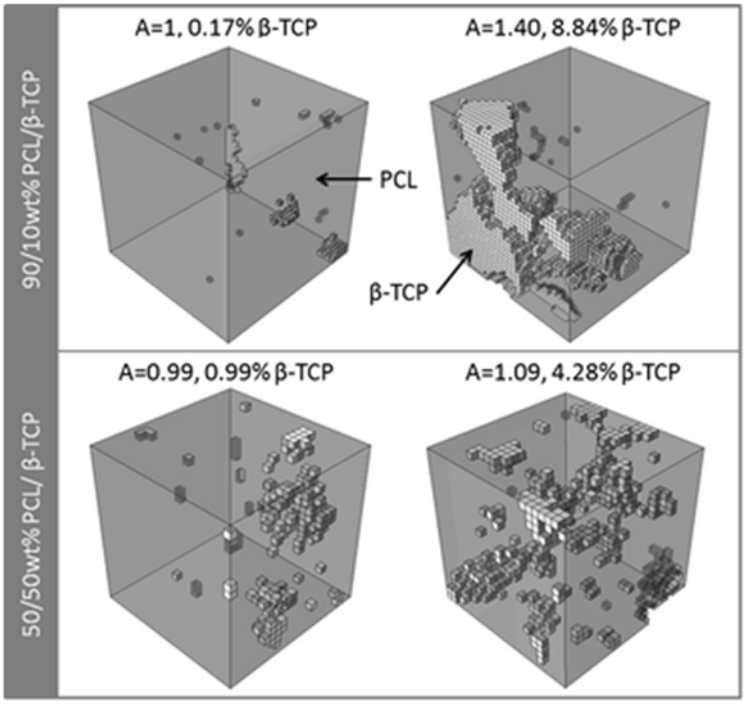

Figure 8: Full strut computational model results for macroscale strut models of 90/10wt% and 50/50wt% PCL/β-TCP struts. Models using the micromechanical-evaluated material properties gave the best approximation of the experimental result (shown in red) for both strut types.